AGU PUBLICATIONS

JGR

Journal of Geophysical Research: Atmospheres

RESEARCH ARTICLE
10.1002/2016JD026020

Key Points:
- Increasing cloud fractions and surface downward longwave flux in spring tend to enhance sea ice melting due to strong cloud warming effect
- Surface shortwave fluxes play a more important role in late spring and early summer than other periods
- Chukchi/Beaufort Sea is important to relate springtime cloud/radiation properties to September sea ice variance at interannual time scale

Correspondence to:
X. Dong,
xdong@email.arizona.edu

Citation:
Huang, Y., X. Dong, B. Xi, E. K. Dolinar, and R. E. Stanfield (2017), The footprints of 16 year trends of Arctic springtime cloud and radiation properties on September sea ice retreat, *J. Geophys. Res. Atmos.*, *122*, 2179–2193, doi:10.1002/2016JD026020.

Received 28 SEP 2016
Accepted 8 FEB 2017
Accepted article online 10 FEB 2017
Published online 21 FEB 2017

The footprints of 16 year trends of Arctic springtime cloud and radiation properties on September sea ice retreat

Yiyi Huang[1], Xiquan Dong[1], Baike Xi[2], Erica K. Dolinar[2], and Ryan E. Stanfield[2]

[1]Department of Hydrology & Atmospheric Sciences, University of Arizona, Tucson, Arizona, USA, [2]Department of Atmospheric Sciences, University of North Dakota, Grand Forks, North Dakota, USA

Abstract The most prominent September Arctic sea ice decline over the period of 2000–2015 occurs over the Siberian Sea, Laptev Sea, and Kara Sea. The satellite observed and retrieved sea ice concentration (SIC) and cloud/radiation properties over the Arctic (70°–90°N) have been used to investigate the impact of springtime cloud and radiation properties on September SIC variation. Positive trends of cloud fractions, cloud water paths, and surface downward longwave flux at the surface over the September sea ice retreat areas are found over the period of 1 March to 14 May, while negative trends are found over the period of 15 May to 28 June. The spatial distributions of correlations between springtime cloud/radiation properties and September SIC have been calculated, indicating that increasing cloud fractions and downward longwave flux during springtime tend to enhance sea ice melting due to strong cloud warming effect. Surface downward and upward shortwave fluxes play an important role from May to June when the onset of sea ice melting occurs. The comparison between linearly detrended and nondetrended of each parameter indicates that significant impact of cloud and radiation properties on September sea ice retreat occurs over the Chukchi/Beaufort Sea at interannual time scale, especially over the period of 31 March to 29 April, while strongest climatological trends are found over the Laptev/Siberian Sea.

1. Introduction

Modeling studies suggest that global climate change signals are expected to be amplified in the Arctic by a factor of 1.5–4.5, which makes it an area of high interest in the research community [*Holland and Bitz*, 2003]. Over the last few decades, the changes in various components of the Arctic climate system have been observed, including surface temperature and albedo, atmospheric circulation, precipitation, snowfall, the biogeochemical cycle, and vegetation [*Wang et al.*, 2012]. Also, the Arctic is very vulnerable to these rapid changes since snow and ice are highly sensitive to changes in surface temperature [*Comiso and Hall*, 2014].

Recent observations have shown dramatic decreases in Arctic sea ice coverage during the remote sensing era from 1979 to present, especially at the end of the melt season. Based on our analyses, the September Arctic (defined as latitudes north of 70°N in this study) sea ice extent (SIE) has been decreasing by roughly 74,961.8 $km^2\,yr^{-1}$ from 1979 to 2015 as demonstrated from the microwave passive remote sensing observations of Nimbus-7 Scanning Multichannel Microwave Radiometer (SSMR); the Defense Meteorological Satellite Program (DMSP)-F8, -F11, and -F13 Special Sensor Microwave/Imagers (SSM/Is); and the DMSP-F17 Special Sensor Microwave Imager/Sounder (SSMIS). Note that the SIE decreases at a higher rate after 2000, and recent years have exhibited record minimum September SIE (e.g., 2007 and 2012) relative to the full satellite record [*Stroeve et al.*, 2015].

The driving forces associated with interannual sea ice variability can be divided into two types, dynamic and thermodynamic. One important dynamical process is the transport of sea ice away from a given location due to regional atmospheric circulation patterns and/or summer storm activities. Surface energy budget anomalies were found to be important drivers for the observed trends and variability of Arctic sea ice [*Serreze et al.*, 2007; *Kapsch et al.*, 2013, 2014]. The cloud-radiation feedback is one of the main contributors for the amplification of Arctic warming [*Curry et al.*, 1996; *Wang et al.*, 2012; *Dong et al.*, 2014; *Comiso and Hall*, 2014; *Pithan and Mauritsen*, 2014]. Several studies have summarized Arctic climate variability and trend from satellite observations. For example, *Parkinson and Cavalieri* [2008] summarized Arctic sea ice variability and trend from 1979 to 2006 according to satellite passive-microwave data for different seasons and regions; *Wang and Key* [2005a, 2005b] identified the spatial and temporal trends of the Arctic surface, cloud, and radiation properties based on the Advanced Very High Resolution Radiometer (AVHRR) Polar Pathfinder (APP) data set from 1982

Table 1. Acronyms and Abbreviations Used in This Study

AOF	Area of Focus
APP-x	Advanced Very High Resolution Radiometer Polar Pathfinder
AVHRR	Advanced very high resolution radiometer
CERES	Clouds and Earth's Radiant Energy System
CF	Cloud fraction
CRE	Cloud radiative effect
CWP	Cloud water path
EBAF	Energy Balanced And Filled
HIY	High sea ice year
LIY	Low sea ice year
LW	Longwave
LW_down flux	Downward longwave flux
LW_up flux	Upward longwave flux
PWV	Precipitable water vapor
MODIS	Moderate Resolution Imaging Spectroradiometer
SIC	Sea ice concentration
SIE	Sea ice extent
SW	Shortwave
SW_down flux	Downward shortwave flux
SW_up flux	Upward shortwave flux
TOA	Top of atmosphere

to 1999. More recently, analysis of the extended APP (APP-x) data set has shown that the Arctic has become warmer and cloudier during the spring and summer over the period of 1982–2004 [*Wang et al*., 2012]. Also, many studies have focused on the impacts of thermodynamic pattern anomalies on Arctic sea ice variability including clouds, atmospheric transport of heat and moisture, and surface radiative and turbulent fluxes [*Jun et al*., 2016; *Kay et al*., 2008; *Kay and Gettleman* 2009]. Specifically, *Choi et al*. [2014] found that anomalies in absorbed solar radiation in the early summer (May–July) have a significant negative correlation ($r \approx -0.8$ with a lag of 1 to 4 months) with the sea ice concentration (SIC) anomalies in late summer (August–October). By using the ERA-Interim reanalysis data set from 1979 to 2010, *Kapsch et al*. [2013] concluded that the greenhouse effect is enhanced by increased cloudiness and humidity, thereby accelerating ice melt. *Devasthale et al*. [2013] discussed the role of increased cloudiness and negative temperature anomalies over the Siberian and Chukchi Sea in summer as a trigger to record minimum SIE in 2012 and made a comparison with the thermodynamic state in 2007. A more recent study has shown that in low sea ice years (LIYs) enhanced positive cloud radiative effect (CRE) in April is followed by decreased negative CRE in May and June through surface-based observations from Barrow, Alaska [*Cox et al*., 2016]. Moreover, based on simulations from the Community Earth System Model, *Kapsch et al*. [2016] found that surface downward longwave (LW_down) flux anomalies in spring and early summer have significant impact on the September SIE, whereas winter anomalies show little effect.

Previous studies are predominately based on surface observations, model simulations, and/or reanalyses or on individual years only. This study aims to provide a comprehensive temporal and spatial analysis of springtime (March–June) cloud and radiation properties using recent satellite retrievals and to examine how these properties relate to September sea ice variation. In particular, this study will focus on the impact of 16 year (2000–2015) linear trends of springtime cloud fraction (CF), cloud water path (CWP), and longwave (LW)/shortwave (SW) fluxes, under all-sky (cloudy + clear-sky) conditions on the September SIC over the Arctic. Note that acronyms and abbreviations used in this study are given in Table 1. Relationships between springtime cloud/radiation properties and September SIC are quantitatively examined to investigate the impact of springtime cloud and radiation properties on September SIC variation. In addition, linearly detrended results are shown to better explain the interannual variability. A sensitivity study has been performed to investigate the contribution of each individual parameter to September SIC variation at interannual time scale.

2. Data and Methodology

In this study, the SIC is obtained from Nimbus-7 SSMR and DMSP SSM/I-SSMIS passive microwave data [*Cavalieri et al*., 1996] version 1 provided by the National Snow and Ice Data Center. SIC is derived from surface brightness temperatures measured from the following sensors: the Nimbus-7 SMMR; the DMSP-F8,

-F11, and -F13 SSM/I; and the DMSP-F17 SSMIS. The data are provided in the polar stereographic projection with a grid cell size of 25 × 25 km from October 1978 to December 2015 at the daily time scale (https://nsidc.org/data/docs/daac/nsidc0051_gsfc_seaice.gd.html). In general, the accuracy of SIC increases when the sea ice is relatively thick and the SIC is high. The uncertainty of SIC over the Arctic is within ±5% during the winter and increases to ±15% during the summer when melt ponds are present on the sea ice [*Cavalieri et al*., 1992].

Cloud properties including CF and CWP used in this study are from the Clouds and Earth's Radiant Energy System (CERES) [*Wielicki et al*., 1996] Moderate Resolution Imaging Spectroradiometer (MODIS) (CERES-MODIS) [*Minnis et al*., 2011a, 2011b] SYN1deg Edition 3A daily gridded data set (1° × 1°) from March 2000 to October 2015, which is derived from both Aqua and Terra satellite measurements. The CF is defined using the CERES-MODIS cloud mask algorithm, which simply equals the cloudy pixels divided by the total (cloudy + clear-sky) pixels. CWP is the sum of liquid water path and ice water path. Liquid water path is retrieved using MODIS cloud pixels identified as liquid and is a product of optical depth and cloud droplet effective radius. Ice water path is retrieved in the same manner using MODIS cloud pixels identified as ice. Further details related to the CERES-MODIS Edition 2 retrieval algorithms for cloud properties can be found in *Minnis et al*. [2011a]. The surface radiation fluxes are from the CERES Energy Balanced And Filled (EBAF)-Surface Edition 2.8 data sets, with daily temporal scale and 1° × 1° spatial resolution. Surface fluxes are computed using the NASA Langley-modified Fu-Liou radiative transfer model with inputs of CERES-MODIS cloud properties and Geostationary Operational Environmental Satellite version 5 atmospheric profiles under the constraint of CERES-observed top-at-atmosphere (TOA) fluxes. The global uncertainties of CERES SYN1deg and CERES EBAF-surface data are summarized by the CERES science team [*CERES_SYN1deg_Ed3A Data Quality Summary*, 2013]. Specifically, *Minnis et al*. [2008] compared CERES-MODIS Aqua and Terra CF retrievals with observations and found a global 7% uncertainty. *Kato et al*. [2013] calculated the biases of EBAF-surface radiation fluxes against 24 surface sites. Surface downward SW (SW_down) flux biases (root-mean-square differences) are given as −1.7 (7.8) Wm^{-2} over land and 4.7 (13.3) Wm^{-2} over the ocean, while LW_down flux biases (root-mean-square differences) are −1.0 (7.6) Wm^{-2} over land and −2.5 (13.3) Wm^{-2} over the ocean [*CERES_EBAF_Ed2.8 Data Quality Summary*, 2014; *CERES_EBAF-Surface_Ed2.8 Data Quality Summary*, 2015]. In particular, *Liu and Key* [2016] found that CF annual cycle from MODIS is uniformly lower than active remote sensor Cloud-Aerosol Lidar and Infrared Pathfinder Satellite Observation by 7.7% over the Arctic. There are other studies comparing the CERES data set with either satellite-retrieved [*Kato et al*., 2012; *Minnis et al*., 2011b] or ground-based observations [*Dong et al*., 2008, 2010; *Xi et al*., 2014], indicating that the CERES data set is good for cloud and radiation study if its uncertainties have been quantified.

Due to the varied spatial resolutions of the satellite products used in this study, SIC data are regridded from their native 25 × 25 km resolution to 1° × 1° grid box to make them comparable to the CERES SYN1deg and CERES EBAF data sets. In this study, we use SIC for spatial distribution comparisons, while SIE is used for describing total amount of sea ice over a region. Our SIE is further filtered as the total area in the Arctic with SICs greater than 15%. The conversion of SIC to SIE is conducted at the daily time scale. In addition, monthly SIEs used in this study are averaged from the daily means. Furthermore, we divide springtime into eight 15 day periods in order to capture short-term variations of each variable from March to June. The 15 day average is calculated from the daily average only if there are more than 10 daily means available for each grid box. Similarly, 16 year linear trends and correlations are calculated when there are more than 10 years of data.

In addition, surface SW and LW CREs are introduced to show the overall effects of cloud and radiation properties on September sea ice retreat, which are calculated using equations (1)–(3) given below. Generally, the CRE is the difference of net radiative fluxes between clear-sky and all-sky conditions. The net CRE is simply the sum of the SW and LW CREs.

$$CRE_{SW} = \left(SW_{all}{}^{\downarrow} - SW^{\uparrow}{}_{all}\right) - \left(SW_{clr}{}^{\downarrow} - SW^{\uparrow}{}_{clr}\right) \quad (1)$$

$$CRE_{LW} = \left(LW^{\downarrow}{}_{all} - LW^{\uparrow}{}_{all}\right) - \left(LW^{\downarrow}{}_{clr} - LW^{\uparrow}{}_{clr}\right) \quad (2)$$

$$CRE_{NET} = CRE_{SW} + CRE_{LW} \quad (3)$$

To quantitatively determine each parameter's contribution to September SIE variation in springtime, the partial correlations between SIE and cloud and radiation properties are calculated using equation (4).

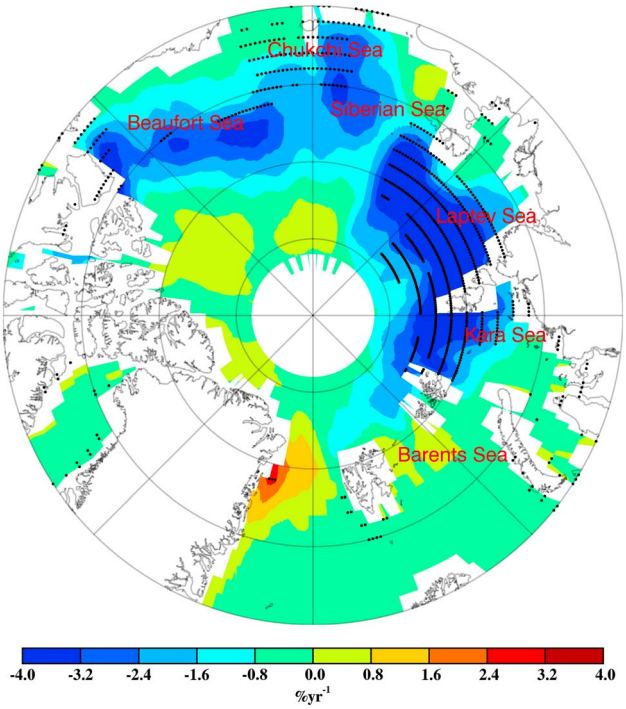

Figure 1. Spatial distribution of 16 year (2000–2015) linear trends of sea ice concentration (SIC) over the Arctic (70°–90°N). The black dots mark the regions where $p < 0.05$ (statistical significant at 95% confidence level; p is the significance of the linear regression).

$$\gamma_{ABC} = \frac{\gamma_{AB} - \gamma_{AC}\,\gamma_{BC}}{\sqrt{(1-\gamma_{AC}^2)(1-\gamma_{BC}^2)}} \quad (4)$$

In equation (4), for example, γ_{ABC} represents the partial correlation between surface net LW flux (A) and September SIE (B) after removing the CF/CWP (C) effect. γ_{AB}, γ_{BC}, and γ_{AC} represent the standard correlations between net LW flux and SIE, CF/CWP and SIE, and CF/CWP and net LW flux, respectively [*Dong et al.*, 2014].

3. The Impacts of Long-Term Linear Trends of Cloud and Radiation Properties on September Sea Ice Retreat

Figure 1 shows the spatial distribution of 16 year linear trends of September SIC over the Arctic. The most prominent September SIC decline during the period of 2000–2015 occurs over the Siberian Sea, Laptev Sea, and Kara Sea, where the sea ice has been retreating on average over 3.2% per year at the 95% confidence level (region marked by black dots). This is consistent with the conclusion of *Kapsch et al.* [2013], where they found that the year-to-year variability in September SIE is most pronounced over the Arctic Ocean north of Siberia from 1979 to 2010 using satellite observations. They defined LIY and high sea ice year (HIY) as year falling outside ±0.5 standard deviations of the linear regression slope, and the SIC anomalies over the Siberian Sea, Laptev Sea, and Kara Sea vary by ~±30% for LIYs and HIYs over the past 30 years.

Figure 2 shows the spatial distributions of 16 year linear trends of CF and CWP. There are two distinguishable changes in CF during the springtime: (a) positive trends of CF are amplified in both magnitude and coverage over the period of 1 March to 14 May from 2000 to 2015 (Figures 2a–2e) and (b) CFs remain nearly constant during the period of 15 May to 28 June (Figures 2f–2h). Comparing Figure 2e with Figure 1, we find that the spatial distribution of the 16 year linear CF trend over the period of 30 April to 14 May is nearly identical to September SIC variation. Similar results have been found in *Wang et al.* [2012] using observations from the extended APP-x satellite data set. They found that the increasing cloudiness during March, April, and May (MAM) occurs primarily in the Arctic Ocean, north of 70°N, at an average annual rate of 0.47% with a standard deviation of 0.12% during the period of 1982–2004. The 16 year CWP trends over the central Arctic Ocean decrease annually over the period of 15 May to 13 June (Figures 2n and 2o). One obvious difference between CF and CWP is that significant negative trends in CWP are found over the Atlantic side of the Arctic during the springtime (March–June), where water vapor is abundant and clouds are optically thicker than those in the ice-covered central Arctic [*Serreze et al.*, 1998]. Note that positive trends of CWP over the Kara Sea and Laptev Sea are found from 16 March to 29 April (Figures 2j–2l). However, in terms of spatial coverage, the increased CWPs are not as large as CFs over the period of 1 March to 14 May, but the decreased CWPs are much larger than CFs over the period of 15 May to 28 June. *Kapsch et al.* [2013] explained that the larger-than-average cloud water and humidity in LIYs primarily attribute to variability of the atmospheric circulation. In particular, *Dong et al.* [2014] found that the onset of the 2007 record low of SIC was triggered by a large-scale atmospheric circulation anomaly during the spring, as strong southerly winds brought more warm and moist air to the region. According to *Wang et al.* [2012], positive trends in the cloud properties from APP-x

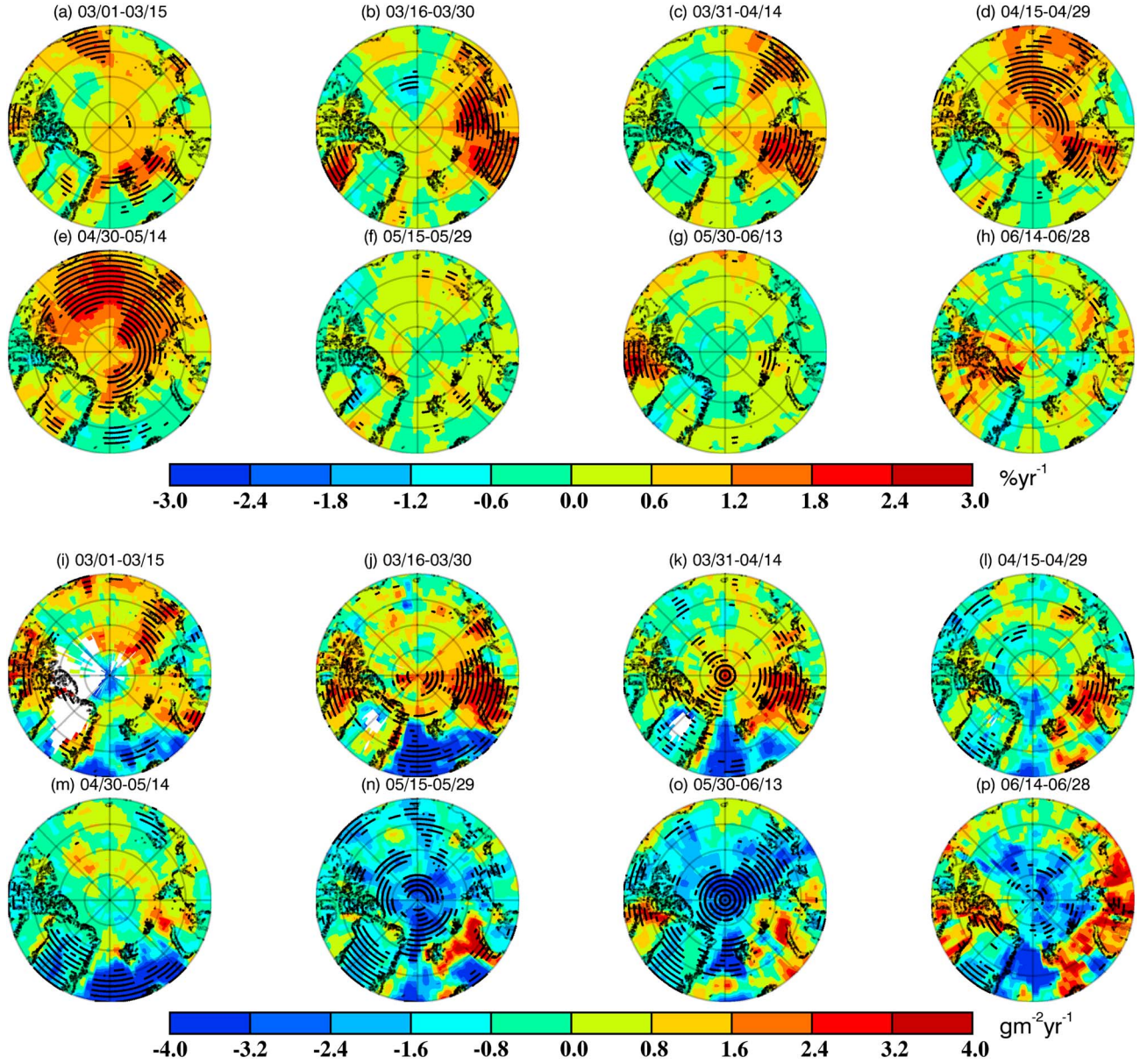

Figure 2. Spatial distribution of the 16 year (2000–2015) linear trends of (a–h) cloud fraction (CF) and (i–p) cloud water path (CWP) over the Arctic (70°–90°N) in eight 15 day time periods from March to June. The black dots mark the regions where $p < 0.05$ (statistical significance at 95% confidence level).

satellite observations in the warm season are generally consistent with the increasing cyclonic activities and total precipitable water vapor (PWV) based on the National Centers for Environmental Prediction/National Center for Atmospheric Research reanalysis data set.

As a primary cause of the cloud warming effect, LW_down flux at the surface annually increases from the central Arctic Ocean to the coasts of Russia over the period of March through mid-May (Figures 3a–3e). The areal coverage of positive LW_down flux trends extends to the Chukchi Sea in the second half of April (Figure 3d), which is much larger than the areas of increased CFs and CWPs. Over the period of 15 May to 28 June, LW_down flux slightly decreases or has minor variations over the Kara Sea, Laptev Sea, and Siberian Sea (Figures 3f–3h), presumably resulting from decreased CFs and CWPs. Spatial distributions of upward LW (LW_up) flux at the surface (not shown) are very similar to those of LW_down flux shown in Figure 3. In contrast, the spatial distributions of SW_down flux at the surface show negative trends from March to mid-May (Figures 3i–3m) and turn to positive trends during the period of 15 May to 28 June (Figures 3n–3p). These changes make physical sense because LW_down/SW_down flux increases/decreases at the surface are

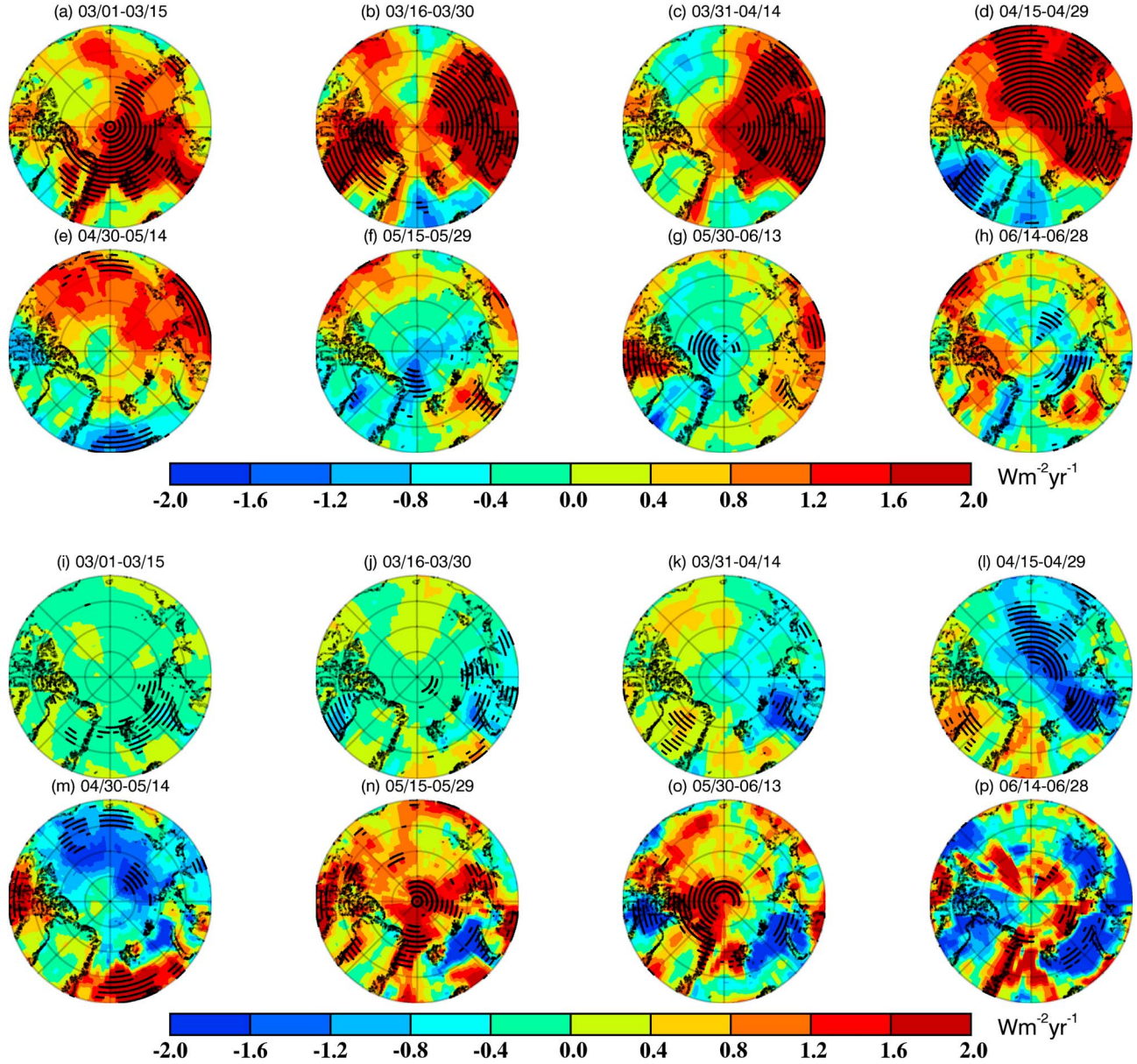

Figure 3. Same as in Figure 2 except for (a–h) all-sky LW_down flux and (i–p) all-sky SW_down flux at the surface.

strongly associated with increased CFs and CWPs, respectively. From 15 April to 14 May (Figures 3l–3m), the negative trends in SW_down flux at the edge of the Arctic Ocean occur simultaneously with increasing CFs, while reduced CWPs tend to increase the SW_down flux over the Atlantic side of Arctic as well as central Arctic Ocean from 30 April to 13 June (Figures 3m–3o). The magnitude of SW fluxes (Figures 3i–3l) cannot compensate that of LW fluxes in early spring (Figures 3a–3d) but is comparable during the middle of spring because of increase of sunlight amount. In addition, SW albedo also plays a significant role in modulating this mechanism after sea ice melting has started and surface albedo is significantly decreased. Based on the results of Figures 2 and 3, we conclude that the trends of SW_down flux are determined by both CF and CWP, while changes of LW_down flux are primarily determined by CF because clouds are generally optically thick. In springtime, the averaged liquid water path over the Arctic is greater than 40 gm^{-2} and the emissivity of clouds is close to one, so that LW_down flux mostly depends on the amount of cloud cover.

The spatial distributions of the correlations between CF and September SIC in each 15 day time period are shown in Figure 4. Generally, the correlations over the areas where the sea ice rapidly decreases turn from

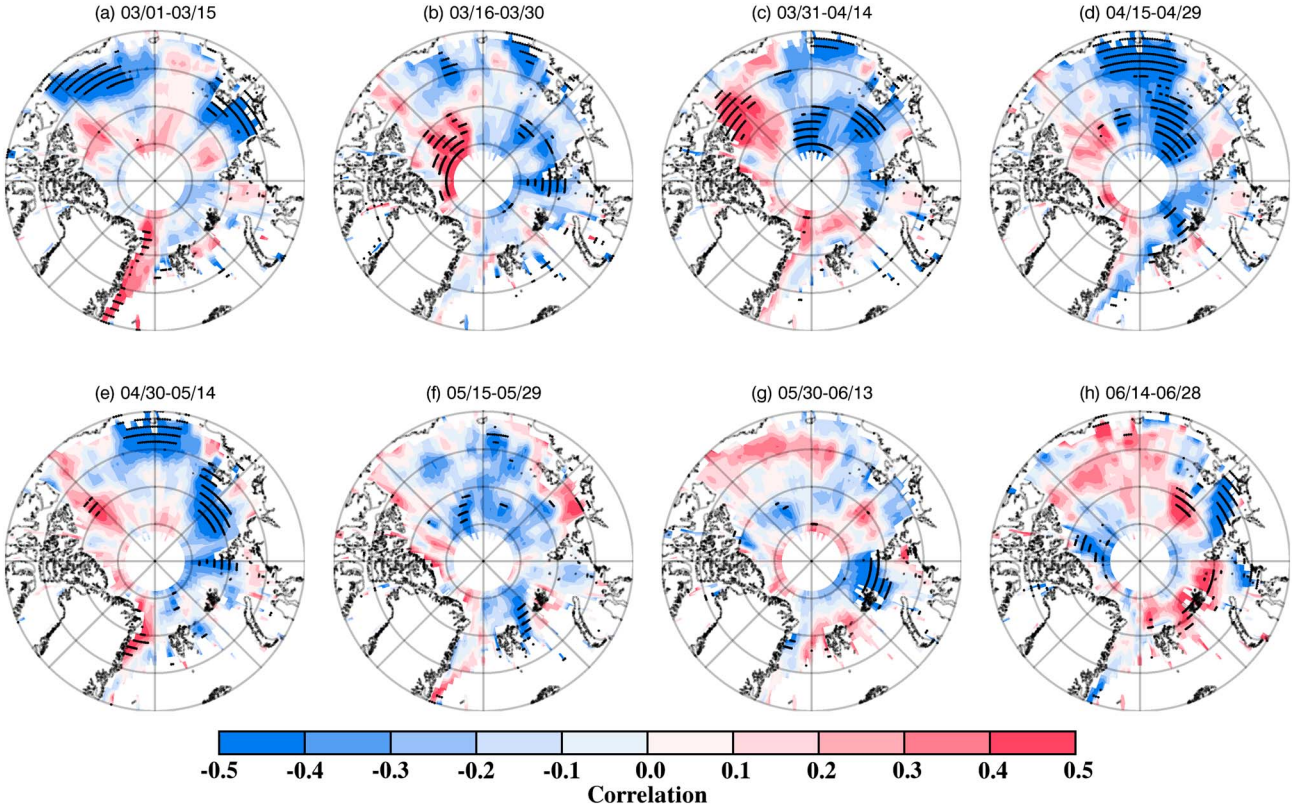

Figure 4. Spatial distribution of correlations between CFs in eight 15 day time periods from March to June and September SIC over the Arctic (70°–90°N). The results are based on 16 years (2000–2015) of data. The black dots mark the regions with $p < 0.1$ (statistical significance at 90% confidence level).

being strongly negative (16 March to 14 May; Figures 4b–4e), slightly negative (15–29 May; Figure 4f), to a mixture of negative and positive (30 May to 13 June; Figure 4g) and strongly positive (14–28 June; Figure 4 h). CWP exhibits a similar pattern to CF, as we found that correlations are negative in March and April and change sign in June (not shown). The strong negative correlations from mid-March to mid-May (Figures 4b–4e) support our conclusion that increasing clouds tends to enhance sea ice melting due to clouds warming effect in spring. As for the areas that show the opposite correlation, they are either largely affected by ocean currents or atmospheric circulation (e.g., the east coast of Greenland) or have relatively higher SIC and little sea ice variations (e.g., Canadian archipelago).

Increasing LW_down flux tends to reduce September SIC by warming the surface from March to mid-May (Figures 5b–5e) over the Kara Sea, Laptev Sea, Siberian Sea, and Chukchi Sea, where the most significant negative SIC trends are found in Figure 1. Similar to CF and CWP, the correlations between springtime LW_down flux and September SIC change sign in mid-May (Figure 5f), indicating that the signals linking September SIC to springtime CF, CWP, and LW fluxes are nearly simultaneous. The gradual change from mostly negative to mostly positive correlations could be well explained by the conclusion in *Cox et al.* [2016]; that is, the cloud-greenhouse (LW) effect is dominant during April (clouds warm surface), while the cloud-albedo (SW) effect is dominant in May and June (clouds cool surface). As mentioned before, the increase of clouds as well as cloud water in LIYs are most likely associated with significantly enhanced transport of warm, moist air in the springtime, which leads to an enhancement of the cloud-greenhouse (LW) effect and further accelerates sea ice melting [*Kapsch et al.*, 2013]. Note that *Choi et al.* [2014] identified a positive correlation between the cloud cover in May and September SIC, which is contradictory to the findings in *Kapsch et al.* [2013]. Furthermore, *Cox et al.* [2016] concluded that timing is a critical factor that can help to explain the discrepancy between these two studies and showed that increased cloud warming in April followed by decreased cloud cooling in May seems to be a significant signal for LIYs. Therefore, our results are in favor of the arguments in *Cox et al.* [2016], who used surface observations from Barrow, Alaska, as we identified the changes of correlation signs in cloud properties as well as LW fluxes from spring (MAM)

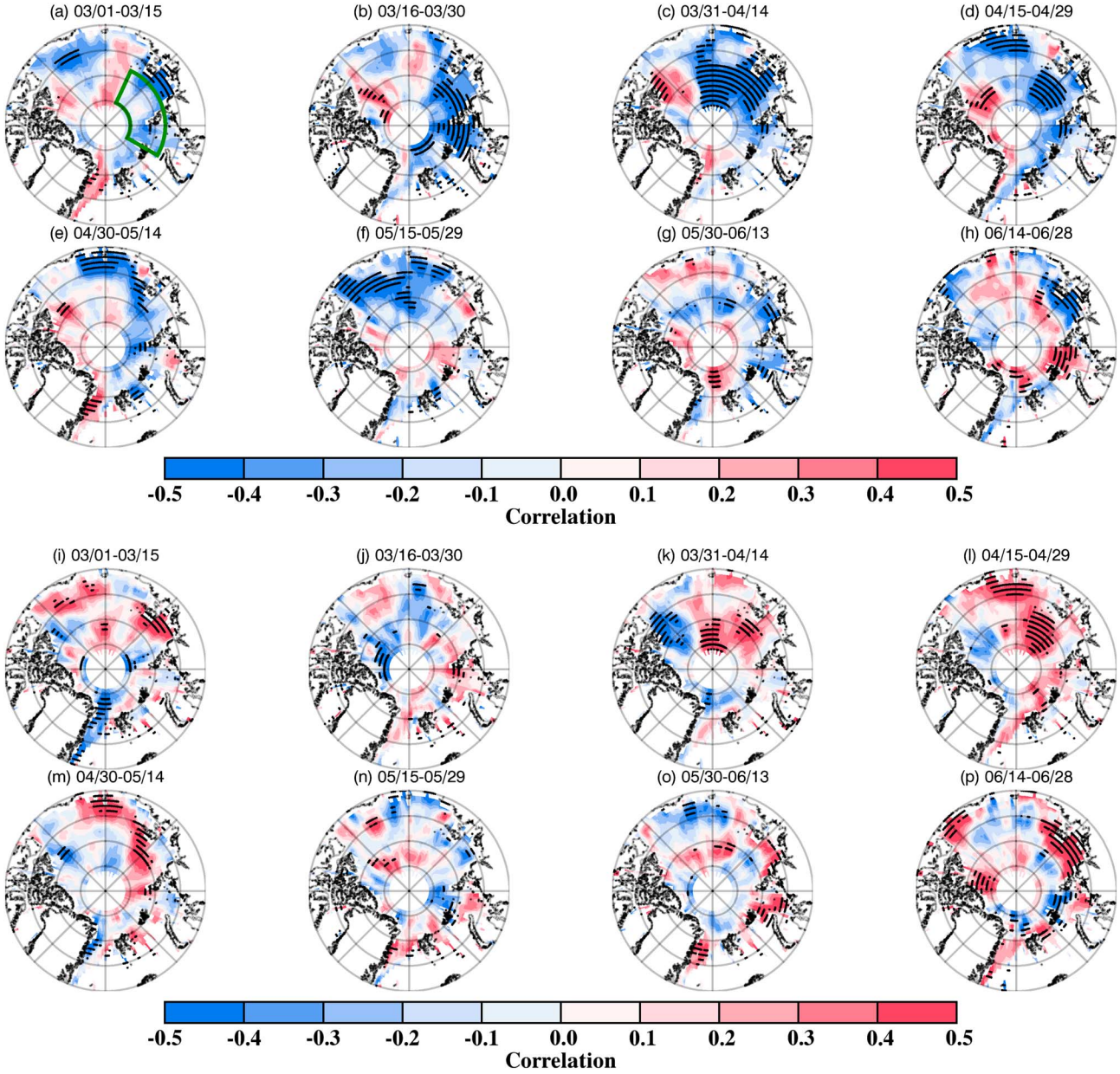

Figure 5. Same as in Figure 4 except for (a–h) all-sky LW_down flux and (i–p) all-sky SW_down flux at the surface.

to early summer (mid-June) over the September sea ice retreat areas. Also, our results are consistent with model simulations in *Kapsch et al*. [2016], which shows that the impact of LW_down flux on September SIC is only evident when surface temperature is lower than but approaches the melting point of snow and ice (e.g., April–May). However, the statistically significant positive correlations between SW_down flux and September SIC can only be found in April (Figures 5k–5m), around 1 month later compared to those of clouds and LW fluxes.

The increase of CF and CWP (Figure 2) over the Arctic leads to increased reflection of incoming solar radiation at the TOA and less solar radiation reaching the surface. The cloud-greenhouse (LW) effect overwhelms the cloud-albedo (SW) effect since cloud and surface albedos are nearly the same, especially during the onset of sea ice melting when CF is high and the surface is mostly covered by snow/ice [*Dong et al*., 2014]. This finding can be also explained by the similar spatial distributions of the correlations between September SIC and CF (Figure 4) and LW_down flux (Figures 5a–5h). In this case, SW_down flux is actually a feedback at the onset

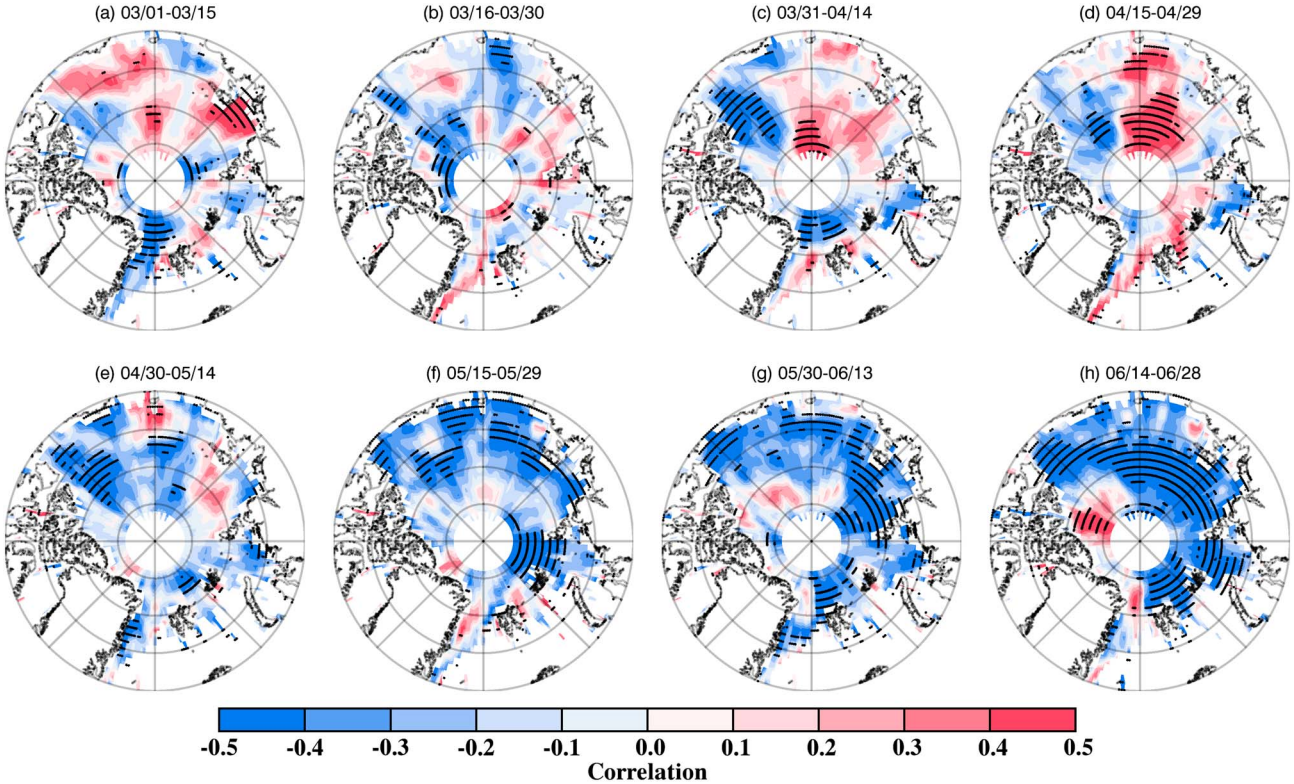

Figure 6. Same as in Figure 4 except for (a–h) all-sky net SW flux at the surface.

of sea ice melt but is not responsible for the initiation of the sea ice anomaly [*Kapsch et al*., 2013; *Dong et al*., 2014]. That is, the changes in cloud properties and LW_down flux during the period of March–April are considered to be the primary causes for September sea ice retreat, while SW_down flux starts to play an important role once sea ice melting has started as surface albedo decreases and more solar radiation is absorbed by the surface [*Dong et al*., 2014; *Mortin et al*., 2016]. Although the correlations between September SIC and SW_down (Figures 5i–5p) and SW_up (not shown) fluxes are not as strong as those between September SIC and springtime LW_down flux, we found that there are distinct negative correlations for net SW flux from mid-May to June over the September sea ice retreat areas (Figures 6f–6h). The positive trends of net SW flux are mainly caused by increased SW_down flux (Figures 3n–3p) due to the decreased cloud properties (Figure 2) and decreased SW_up flux resulting from the initiation of sea ice melting. These results confirm the conclusion in *Kapsch et al*. [2013] that the net SW flux anomaly becomes positive around mid-May when sea ice melting begins and the surface albedo decreases.

4. The Impacts of Interannual Variability of Cloud and Radiation Properties on September Sea Ice Retreat

In order to eliminate the overall effects of climate change and better explain interannual variability, correlation patterns between linearly detrended surface net CRE and September SIC are shown (Figures 7i–7p) for comparison with nondetrended results (Figures 7a–7h). We found that September SIC has a strong negative correlation with surface net CRE from mid-March to April (Figures 7b–7d) and becomes slightly positive in May (Figures 7e and 7f). Comparing Figures 7a–7h with Figures 4 and 5, the correlation patterns of surface net CREs are similar to those of CF and LW_down flux from mid-March through April, while matching closer to SW_down flux during late spring and early summer. This result supports our conclusion that surface SW fluxes tend to be more important in the late spring. However, when we compare the detrended and nondetrended correlation patterns over the September sea ice retreat areas, we found that they match closely over the Chukchi/Beaufort Sea (area of focus (AOF)2: 74°–84°N, 160°–210°E; outlined in yellow) but not over the Laptev/Siberian Sea (AOF1: 78°–85°N, 60°–155°E; outlined in green). For example, significant negative

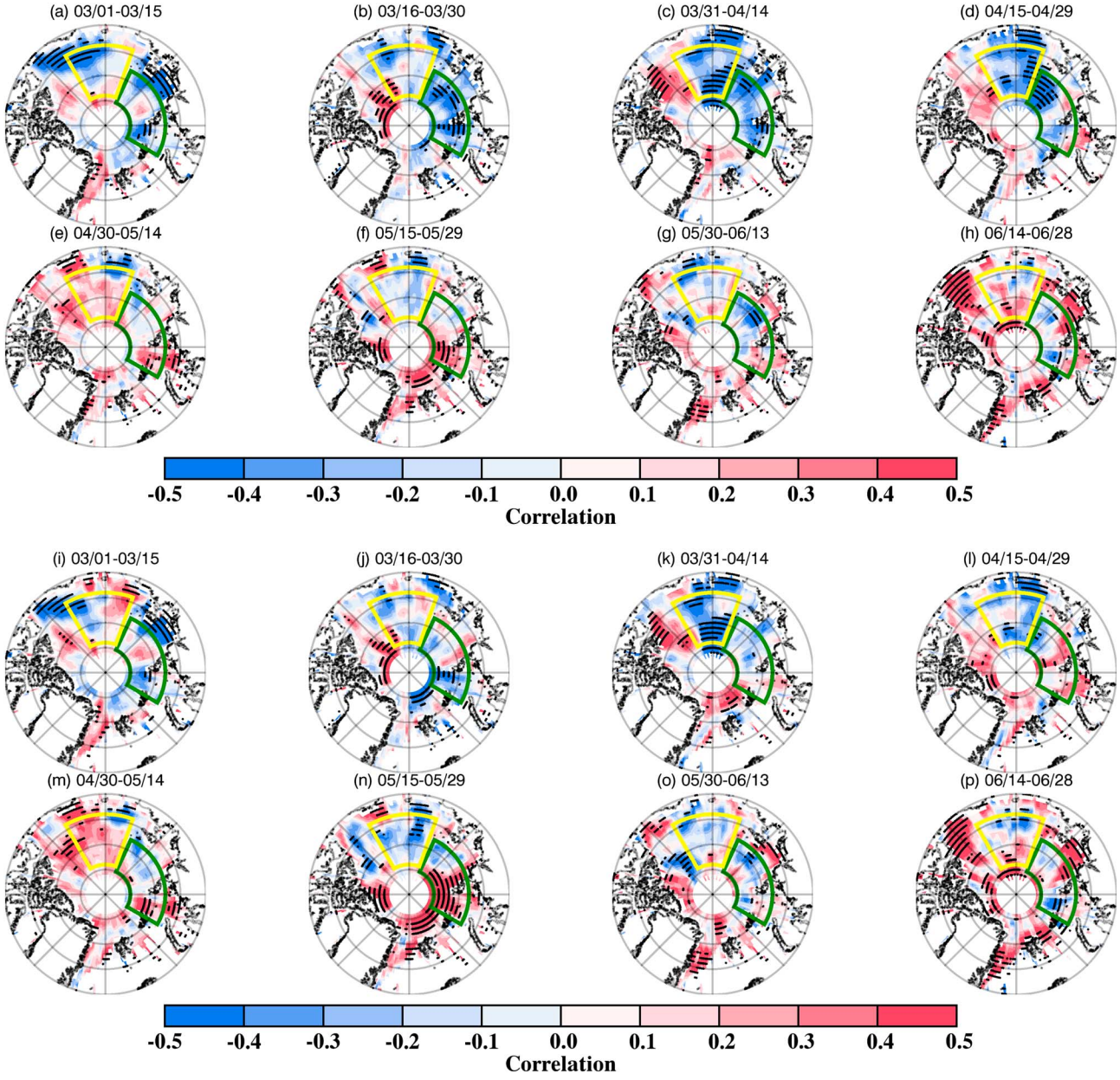

Figure 7. Same as in Figure 4 except for (a–h) net CRE and (i–p) linearly detrended net CRE at the surface. The area of focus 1 (AOF1; 78°–85°N, 60°–155°E) is outlined in green, and AOF2 (74°–84°N, 160°–210°E) is outlined in yellow.

correlations over the AOF1 during 16 March to 29 April become much weaker after detrending data. It means that large part of the correlations between cloud/radiation properties and September SIC over this region should be explained by long-term trends instead of interannual variability, although this region shows the most significant negative trends of September sea ice.

To investigate the climatological patterns more closely for these two regions, the 16 year anomalies of cloud and radiation properties and their linear trends within the AOF1 (Figures 8b–8g) are chosen to diagnose possible synchronous variations with SIE anomaly in Figure 8a. Note that we have identified different time periods in Figure 8 for each parameter based on the results from Figures 4–6 and shown them at the top right corner of each plot in order to demonstrate the largest correlations with September SIE over the period of March–June. As illustrated in Figures 8b and 8c, both CFs and CWPs within the AOF1 during the period of 16 March to 14 April increase at a rate of 1.14% yr^{-1} and 1.46 gm^{-2} yr^{-1}, respectively, with moderate

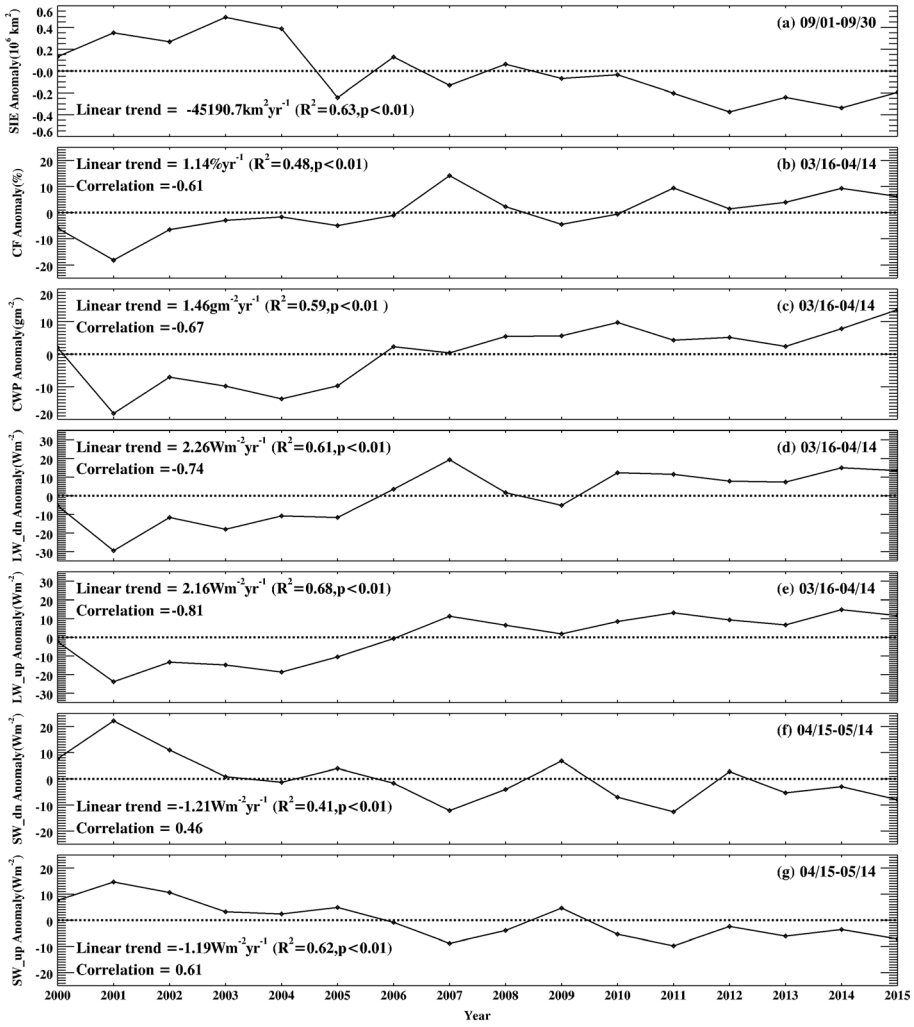

Figure 8. The 16 year (2000–2015) anomalies with respect to the average of (a) September SIE, (b) CF, (c) CWP, (d) surface all-sky LW_down flux, (e) surface all-sky LW_up flux, (f) surface all-sky SW_down flux, and (g) surface all-sky SW_up flux over the AOF1. Note that the values of cloud and radiation properties are averaged within the time period (30 days) shown in each plot. The linear trends are provided for each variable with their coefficients of determination (R^2) and confidence level (p). The correlations between cloud and radiation properties and September SIE are shown as well.

negative correlations of −0.61 and −0.67 with September SIE. These results indicate that the increases of springtime CF and CWP can enhance sea ice retreat. Similarly, both LW_down and LW_up fluxes at the surface increase by ~2 $Wm^{-2}yr^{-1}$ during the 16 year period, with negative correlations of −0.74 and −0.81, respectively, with September SIE. As discussed before, the contributions of springtime cloud properties and LW fluxes to September SIE are nearly simultaneous (March–April). However, the long-term trends we found over the AOF2 are not as significant as those over the AOF1 (not shown). In this case, we conclude that the AOF1 shows most significant climatological trends of cloud/radiation properties during the springtime, while the AOF2 is more important to relate the impact of springtime cloud/radiation properties on September sea ice retreat at interannual time scale.

Therefore, a sensitivity study has been conducted to investigate how much each parameter during the springtime can contribute to September SIE over the AOF2 based on linearly detrended data. The regression slopes ($\delta SIE/\delta()$), coefficients of determination (R^2), and confidence level (p) between springtime cloud/radiation properties and September SIE are shown in Table 2, and p values less than 0.20 are marked in bold as statistically significant (at the 80% confidence level). Note that these are not independent variables, so that the values shown here are used to make the comparison for different time periods

Table 2. The Regression Slopes, δSIE/δ(), Coefficients of Determination (R^2), and Confidence Level (p) Between Cloud and Radiation Properties and September SIE Over the AOF2 in Eight 15 Day Time Periods From March to June[a]

Time Period		01/03 to 15/03	16/03 to 30/03	31/03 to 14/04	15/04 to 29/04	30/04 to 14/05	15/05 to 29/05	30/05 to 13/06	14/06 to 28/06
Cloud fraction	δSIE/δ()[b]	5,974.7	−61.2	**−7,118.7**	**−14,195.1**	3,656.6	−3,355.1	**6,663.9**	2,758.8
	R^2	0.093	0.000	**0.168**	**0.446**	0.025	0.014	**0.174**	0.031
	p	0.250	0.991	**0.115**	**0.005**	0.559	0.667	**0.108**	0.511
Cloud water path	δSIE/δ()[c]	−3,234.8	**6,092.0**	−6,353.0	2,521.4	**7,325.3**	4,444.4	**4,316.0**	2,370.0
	R^2	0.059	**0.151**	0.043	0.023	**0.147**	0.070	**0.152**	0.072
	p	0.366	**0.137**	0.441	0.573	**0.143**	0.324	**0.136**	0.316
Surface LW_dn	δSIE/δ()[d]	**5,859.7**	3,447.9	**−6,149.6**	−3,890.9	617.9	**−8,075.1**	6,560.7	4,957.3
	R^2	**0.209**	0.065	**0.235**	0.049	0.002	**0.190**	0.063	0.041
	p	**0.075**	0.339	**0.057**	0.412	0.878	**0.092**	0.347	0.450
Surface LW_up	δSIE/δ()[d]	**10,258.9**	3,524.22	**−6,735.5**	4,263.7	423.8	**−19,016.3**	−51,013.0	−110,119.0
	R^2	**0.319**	0.043	**0.120**	0.028	0.000	**0.321**	0.112	0.072
	p	**0.023**	0.440	**0.188**	0.533	0.948	**0.022**	0.204	0.314
Surface net LW	δSIE/δ()[d]	4,517.2	9,496.3	**−11,220.9**	**−13,314.3**	1,474.5	−6,017.8	7,680.5	5,493.1
	R^2	0.021	0.065	**0.227**	**0.254**	0.003	0.039	0.091	0.048
	p	0.596	0.341	**0.062**	**0.046**	0.838	0.462	0.257	0.414
Surface LW CRE	δSIE/δ()[d]	10,588.3	2,562.4	**−13,694.8**	**−20,872.2**	4,487.7	−6,121.0	**12,012.9**	4,560.4
	R^2	0.079	0.005	**0.239**	**0.435**	0.024	0.024	**0.269**	0.037
	p	0.292	0.791	**0.054**	**0.005**	0.565	0.565	**0.039**	0.474
Surface SW_dn	δSIE/δ()[d]	−10,014.6	−11,303.7	**11,566.6**	**12,026.3**	−3,502.3	−1,060.6	−3,936.2	−646.3
	R^2	0.010	0.061	**0.175**	**0.250**	0.040	0.002	0.101	0.003
	p	0.709	0.358	**0.107**	**0.048**	0.459	0.857	0.230	0.832
Surface SW_up	δSIE/δ()[d]	525.0	−14,585.6	**17,978.1**	**10,023.4**	−1,388.8	5,226.5	5,818.0	**5,644.8**
	R^2	0.000	0.029	**0.145**	**0.123**	0.003	0.029	0.108	**0.217**
	p	0.993	0.525	**0.146**	**0.182**	0.843	0.527	0.214	**0.069**
Surface net SW	δSIE/δ()[d]	−25,626.0	−23,199.5	**18,882.1**	**41,850.4**	**−15,176.7**	−12,977.1	**−11,901.2**	**−7,723.5**
	R^2	0.026	0.077	**0.136**	**0.350**	**0.139**	0.102	**0.526**	**0.336**
	p	0.547	0.298	**0.160**	**0.016**	**0.156**	0.228	**0.001**	**0.019**
Surface SW CRE	δSIE/δ()[d]	−3,673.5	**−81,022.5**	**50,193.3**	**42,835.5**	−8,589.6	−5,543.8	**−9,681.8**	−3,840.2
	R^2	0.000	**0.148**	**0.177**	**0.358**	0.038	0.022	**0.209**	0.038
	p	0.989	**0.141**	**0.104**	**0.014**	0.468	0.582	**0.075**	0.469
Surface net CRE	δSIE/δ()[d]	10,398.0	357.4	**−17,542.4**	**−32,609.2**	3,946.1	**−39,888.6**	5,019.3	−7,995.2
	R^2	0.077	0.000	**0.243**	**0.406**	0.003	**0.319**	0.005	0.014
	p	0.299	0.974	**0.052**	**0.008**	0.831	**0.023**	0.799	0.663

[a]The results are based on 16 years (2000–2015) of linearly detrended data. The results with $p < 0.20$ are marked in bold (statistical significance at 80% confidence level).
[b]The unit is $km^2\ \%^{-1}$.
[c]The unit is $km^2\ (gm^{-2})^{-1}$.
[d]The unit is $km^2\ (Wm^{-2})^{-1}$.

instead of across different variables. We found that the significant regression slopes occur almost all of the cloud and radiation variables except CWP over the period of 31 March to 29 April. Specifically, the most significant contribution of net LW flux to the total variance of September SIE is ~25% over the period of 15 April to 29 April, while net SW flux mostly contributes to the September SIE variance by ~53% over the period of 30 May to 13 June.

To quantitatively determine each springtime parameter's contribution to September SIE variation, partial correlations between SIE and cloud/radiation properties over the AOF2 have been calculated based on linearly detrended data as listed in Table 3. To calculate partial correlations of CF and CWP with September SIE, the net LW and SW flux effects have been removed and vice versa; the CF and CWP effects have been removed when calculating partial correlations of LW and SW fluxes. Note that we use net radiative fluxes instead of each individual radiative parameter to reduce the interactions between downward and upward radiation fluxes. Interestingly, the partial correlations tend to be more significant (marked in bold) over the period of 16 March to 30 March for all variables, during which the strongest negative partial correlations of CF and positive partial correlations of net LW flux are found. As expected, the negative correlations between net SW flux and September SIE are slightly enhanced after removing cloud effects in June, indicating that SW flux also tends to be more important once sea ice melting has started in late spring and early summer at interannual time scale.

Table 3. Standard and Partial Correlations of CF (Removing Net LW and SW Fluxes), CWP (Removing Net LW and SW Fluxes), Net All-Sky LW Flux (Removing CF and CWP), and Net All-Sky SW Flux (Removing CF and CWP) With September SIE in Eight 15 Day Time Periods From March to June Over the AOF2[a]

Time Period		01/03 to 15/03	16/03 to 30/03	31/03 to 14/04	15/04 to 29/04	30/04 to 14/05	15/05 to 29/05	30/05 to 13/06	14/06 to 28/06
Cloud fraction	Standard	0.305	−0.003	**−0.410**	**−0.668**	0.158	−0.117	**0.417**	0.177
	Partial	0.349	**−0.509**	−0.068	**−0.500**	0.165	−0.277	−0.291	−0.459
Cloud water path	Standard	−0.242	**0.388**	−0.207	0.153	**0.383**	0.264	**0.390**	0.268
	Partial	−0.277	**0.421**	−0.226	0.207	0.150	−0.063	−0.278	0.108
Surface net LW flux	Standard	0.144	0.251	**−0.478**	**−0.505**	0.055	−0.200	0.303	0.255
	Partial	−0.172	**0.630**	−0.306	0.310	−0.257	−0.070	−0.149	0.024
Surface net SW flux	Standard	−0.163	−0.281	**0.364**	**0.600**	**−0.376**	−0.318	**−0.726**	**−0.580**
	Partial	0.223	**−0.410**	−0.020	0.343	−0.337	−0.252	**−0.735**	**−0.715**

[a]The results are based on 16 years (2000–2015) of linearly detrended data. The results with $p < 0.20$ are marked in bold (statistical significance at 80% confidence level).

5. Summary and Conclusions

Satellite data sets have been used to investigate the impact of springtime (March–June) cloud and radiation properties on September SIC variation over the Arctic from 2000 to 2015. The long-term trends and interannual variability have been discussed separately to relate springtime cloud and radiation properties with September sea ice retreat. At interannual time scale, a sensitivity study has also been performed to investigate the contribution of each individual parameter in springtime in regards to September sea ice variation. Through an integrative analysis of springtime cloud and radiation properties and their correlations with September SIC within 16 years, we have drawn the following conclusions:

1. Positive trends of CF and CWP over the September sea ice retreat areas are found over the period of 1 March to 14 May, while negative trends are found over the period of 15 May to 28 June. Increased CWPs over the Arctic are not as large as CFs in coverage over the period of 1 March to 14 May, but decreased CWPs are much larger than CFs over the period of 15 May to 28 June. As a primary cause of cloud warming effects, surface LW_down flux increases annually from the central Arctic Ocean to the coast of Russia from March to mid-May, while surface SW_down flux decreases during the same time period. From this study we found that the trends of SW_down flux at the surface are related to both CF and CWP, while changes of surface LW_down flux are primarily determined by CF.
2. Spatial distributions of the correlations between springtime cloud and radiation properties and September SIC have been calculated. Both CF and CWP over the September sea ice retreat areas have relatively strong negative correlations with September SIC from mid-March to mid-May, indicating that increasing CF and surface LW_down flux during the springtime tend to enhance sea ice melting due to strong cloud warming effect. From this study, we found that the cloud-greenhouse (LW) effect overwhelms the cloud-albedo (SW) effect during the springtime. More specifically, changes in cloud properties and surface LW_down flux over the period of March-April are primarily responsible for September sea ice retreat, while SW fluxes at the surface tend to be more important over the period of May–June.
3. The correlation patterns of net CRE between linearly detrended and nondetrended properties indicate that significant impacts of springtime cloud and radiation properties on September sea ice variance occur over the Chukchi/Beaufort Sea (AOF2) at interannual time scale, especially over the period of 31 March to 29 April, while strongest climatological trends are found over the Laptev/Siberian Sea (AOF1). And the partial correlations tend to be more significant over the period of 16 March to 30 March for all variables.

We understand that although the clouds and radiation budgets in the Arctic play very important roles in determining sea ice variations in September, other thermodynamic variables (e.g., surface air temperature, PWV, and sensible/latent heat) and dynamic factors (e.g., atmospheric circulation pattern, summer storm activity, and ocean current) should not be neglected [*Serreze et al.*, 2007; *Kapsch et al.*, 2013; *Dong et al.*, 2014; *Parkinson and Comiso*, 2013; *Zhang et al.*, 2013]. Seasonal sea ice forecasts could be improved by a more

comprehensive investigation of diverse thermodynamic and dynamic influences by using both observations and model simulations in the future.

Acknowledgments
This study was supported by NOAA MAPP under grant NA13OAR4310105 at the University of North Dakota and NASA CERES project under grant NNX17AC52G at the University of Arizona. Sea ice concentrations from Nimbus-7 SMMR and DMSP SSM/I-SSMIS Passive Microwave Data, version 1, are accessed from NASA DAAC at the National Snow and Ice Data Center at http://nsidc.org/data/docs/daac/nsidc0051_gsfc_seaice.gd.html#cavalieri_92, while NASA CERES SYN1deg and CERES EBAF-surface data sets are available at http://ceres.larc.nasa.gov/order_data.php. We would like to thank Benjamin Herman for proofreading this manuscript. Also, we appreciate three anonymous reviewers for their constructive comments and suggestions.

References

Cavalieri, D. J., et al. (1992), NASA Sea Ice Validation Program for the DMSP SSM/I: Final report, NASA Technical Memorandum 104559, Natl. Aeronautics and Space Administration, Washington, D. C. 126 p.

Cavalieri, D., C. Parkinson, P. Gloersen, and H. J. Zwall (1996), Sea ice concentrations from Nimbus-7 SMMR and DMSP SSM/I-SSMIS Passive Microwave Data, version 1, Boulder, Colo. NASA DAAC at the Natl. Snow and Ice Data Center. [Available at 10.5067/8GQ8LZQVL0VL].

CERES_EBAF_Ed2.8 Data Quality Summary (2014). [Available at http://ceres.larc.nasa.gov/documents/DQ_summaries/CERES_EBAF_Ed2.8_DQS.pdf]

CERES_EBAF-Surface_Ed2.8 Data Quality Summary (2015). [Available at http://ceres.larc.nasa.gov/documents/DQ_summaries/CERES_EBAF-Surface_Ed2.8_DQS.pdf]

CERES_SYN1deg_Ed3A Data Quality Summary (2013). [Available at http://ceres.larc.nasa.gov/documents/DQ_summaries/CERES_SYN1deg-lite_Ed2.6_DQS.pdf]

Choi, Y. S., B. M. Kim, S. K. Hur, S. J. Kim, J. H. Kim, and C. H. Ho (2014), Connecting early summer cloud-controlled sunlight and late summer sea ice in the Arctic, *J. Geophys. Res. Atmos.*, *119*, 11,087–11,099, doi:10.1002/2014JD022013.

Comiso, J. C., and D. K. Hall (2014), Climate trends in the Arctic as observed from space, *Wiley Interdiscip. Rev.: Clim. Change*, *5*(3), 389–409.

Cox, C. J., T. Uttal, C. N. Long, M. D. Shupe, R. S. Stone, and S. Starkweather (2016), The role of springtime arctic clouds in determining autumn sea ice extent, *J. Clim.*, doi:10.1175/JCLI-D-16-0136.1.

Curry, J. A., J. L. Schramm, W. B. Rossow, and D. Randall, (1996), Overview of Arctic cloud and radiation characteristics, *J. Clim.*, *9*, 1731–1764, doi:10.1175/1520-0442(1996)009<1731:OOACAR>2.0.CO;2.

Devasthale, A., J. Sedlar, T. Koenigk, and E. J. Fetzer (2013), The thermodynamic state of the Arctic atmosphere observed by AIRS: Comparisons during the record minimum sea ice extents of 2007 and 2012, *Atmos. Chem. Phys.*, *13*(15), 7441–7450.

Dong, X., P. Minnis, B. Xi, S. Sun-Mack, and Y. Chen (2008), Comparison of CERES-MODIS stratus cloud properties with ground-based measurements at the DOE ARM Southern Great Plains site, *J. Geophys. Res.*, *113*, D03204, doi:10.1029/2007JD008438.

Dong, X., B. Xi, K. Crosby, C. N. Long, R. Stone, and M. Shupe (2010), A 10-yr climatology of arctic cloud fraction and radiative forcing at barrow, Alaska, *J. Geophys. Res.*, *115*, D12124, doi:10.1029/2009JD013489.

Dong, X., B. J. Zib, B. Xi, R. Stanfield, Y. Deng, X. Zhang, B. Lin, and C. N. Long (2014), Critical mechanisms for the formation of extreme arctic sea-ice extent in the summers of 2007 and 1996, *Clim. Dyn.*, *43*, 53–70, doi:10.1007/s00382-013-1920-8.

Holland, M. M., and C. M. Bitz (2003), Polar amplification of climate change in coupled models, *Clim. Dyn.*, *21*(3–4), 221–232, doi:10.1007/s00382-003-0332-6.

Jun, S. Y., C. H. Ho, J. H. Jeong, Y. S. Choi, and B. M. Kim (2016), Recent changes in winter Arctic clouds and their relationships with sea ice and atmospheric conditions, *Tellus A*, *68*, 29,130, doi:10.3402/tellusa.v68.29130.

Kapsch, M. L., R. G. Graversen, and M. Tjernström (2013), Springtime atmospheric energy transport and the control of Arctic summer sea-ice extent, *Nat. Clim. Change*, *3*, 744–748, doi:10.1038/nclimate1884.

Kapsch, M. L., R. G. Graversen, T. Economou, and M. Tjernström (2014), The importance of spring atmospheric conditions for predictions of the Arctic summer sea ice extent, *Geophys. Res. Lett.*, *41*, 5288–5296, doi:10.1002/2014GL060826.

Kapsch, M. L., R. G. Graversen, M. Tjernström, and R. Bintanja (2016), The effect of downwelling longwave and shortwave radiation on Arctic summer sea ice, *J. Clim.*, *29*(3), 1143–1159.

Kato, S., N. G. Loeb, D. A. Rutan, F. G. Rose, S. Sun-Mack, W. F. Miller, and Y. Chen (2012), Uncertainty estimate of surface irradiances computed with MODIS-, CALIPSO-, and CloudSat-derived cloud and aerosol properties, *Surv. Geophys.*, *33*, 395–412, doi:10.1007/s10712-012-9179-x.

Kato, S., et al. (2013), Surface irradiances consistent with CERES-derived top-of-atmosphere shortwave and longwave irradiances, *J. Clim.*, *26*, 2719–2740, doi:10.1175/JCLI-D-12-00436.1.

Kay, J. E., and A. Gettleman (2009), Cloud influence on and response to seasonal Arctic sea ice loss, *J. Geophys. Res.*, *114*, D18204, doi:10.1029/2009JD011773.

Kay, J. E., T. L'Ecuyer, A. Gettelman, G. Stephens, and C. O'Dell (2008), The contribution of cloud and radiation anomalies to the 2007 Arctic sea ice extent minimum, *Geophys. Res. Lett.*, *35*, L08503, doi:10.1029/2008GL033451.

Liu, Y., and J. R. Key (2016), Assessment of Arctic cloud cover anomalies in atmospheric reanalysis products using satellite data, *J. Clim.*, *29*(17), 6065–6083.

Minnis, P., et al. (2008), Cloud detection in non-polar regions for CERES using TRMM VIRS and Terra 615 and Aqua MODIS data, *IEEE Trans. Geosci. Remote Sens.*, *46*, 3857–3884.

Minnis, P., et al. (2011a), CERES edition-2 cloud property retrievals using TRMM VIRS and Terra and Aqua MODIS data—Part I: Algorithms, *IEEE Trans. Geosci. Remote Sens.*, *49*, 4374–4400, doi:10.1109/TGRS.2011.2144601.

Minnis, P., et al. (2011b), CERES edition-2 cloud property retrievals using TRMM VIRS and Terra and Aqua MODIS data—Part II: Examples of average results and comparisons with other data. Geoscience and Remote Sensing, *IEEE Trans. Geosci. Remote Sens.*, *49*, 4401–4430, doi:10.1109/TGRS.2011.2144602.

Mortin, J., G. Svensson, R. G. Graversen, M. L. Kapsch, J. C. Stroeve, and L. N. Boisvert (2016), Melt onset over Arctic sea ice controlled by atmospheric moisture transport, *Geophy. Res. Lett.*, *43*, 6636–6642, doi:10.1002/2016GL069330.

Parkinson, C. L., and D. J. Cavalieri (2008), Arctic sea ice variability and trends, 1979–2006, *J. Geophys. Res.*, *113*, C07003, doi:10.1029/2007JC004558.

Parkinson, C. L., and J. C. Comiso (2013), On the 2012 record low Arctic sea ice cover: Combined impact of preconditioning and an August storm, *Geophys. Res. Lett.*, *40*, 1356–1361, doi:10.1002/grl.50349.

Pithan, F., and T. Mauritsen (2014), Arctic amplification dominated by temperature feedbacks in contemporary climate models, *Nat. Geosci.*, *7*(3), 181–184, doi:10.1038/ngeo2071.

Serreze, M. C., J. R. Key, J. E. Box, J. A. Maslanik, and K. Steffen (1998), A new monthly climatology of global radiation for the Arctic and comparisons with NCEP-NCAR reanalysis and ISCCP-C2 fields, *J. Clim.*, *11*(2), 121–136, doi:10.1175/1520-0442(1998)011<0121:ANMCOG>2.0.CO;2.

Serreze, M. C., M. M. Holland, and J. Stroeve (2007), Perspectives on the Arctic's shrinking sea-ice cover, *Science*, *315*, 1533–1536, doi:10.1126/science.1139426.

Stroeve, J., E. Blanchard-Wrigglesworth, V. Guemas, S. Howell, F. Massonnet, and S. Tietsche (2015), Improving predictions of Arctic sea ice extent, *Eos Trans. AGU*, *96*, doi:10.1029/2015EO031431.

Wang, X., and J. R. Key (2005a), Arctic surface, cloud, and radiation properties based on the AVHRR Polar Pathfinder dataset. Part I: Spatial and temporal characteristics, *J. Clim.*, *18*(14), 2558–2574, doi:10.1175/JCLI3438.1.

Wang, X., and J. R. Key (2005b), Arctic surface, cloud, and radiation properties based on the AVHRR Polar Pathfinder dataset. Part II: Recent trends, *J. Clim.*, *18*(14), 2575–2593, doi:10.1175/JCLI3439.1.

Wang, X., J. R. Key, Y. Liu, C. Fowler, J. Maslanik, and M. Tschudi (2012), Arctic climate variability and trends from satellite observations, *Adv. Meteorol.*, *2012*, doi:10.1155/2012/505613.

Wielicki, B. A., B. R. Barkstrom, E. F. Harrison, R. B. Lee III, G. L. Smith, and J. E. Cooper (1996), Clouds and the Earth's Radiant Energy System (CERES): An Earth Observing System experiment, *Bull. Am. Meteorol. Soc.*, *77*, 853–868.

Xi, B., X. Dong, P. Minnis, and S. Sun-Mack (2014), Comparison of marine boundary layer cloud properties from CERES-MODIS edition 4 and DOE ARM AMF measurements at the Azores, *J Geophys. Res. Atmos.*, *119*, 9509–9529, doi:10.1002/2014JD021813.

Zhang, J., R. Lindsay, A. Schweiger, and M. Steele (2013), The impact of an intense summer cyclone on 2012 Arctic sea ice retreat, *Geophys. Res. Lett.*, *40*, 720–726, doi:10.1002/grl.50190.